Hydrodynamic efficient cell capture and pairing method on microfluidic cell electrofusion chip 🄵

View Online   Export Citation   CrossMark

Xuefeng Wang,[1] 🄳 Yaqi Bai,[1] 🄳 Xiaoling Zhang,[2] 🄳 Wei Li,[1] Jun Yang,[1] 🄳 and Ning Hu[1,a] 🄳

AFFILIATIONS

[1]Key Laboratory of Biorheological Science and Technology, Ministry of Education and Bioengineering College, Chongqing University, Chongqing 400044, China
[2]School of Smart Health, Chongqing College of Electronic Engineering, Chongqing 401331, China

[a]Author to whom correspondence should be addressed: huning@cqu.edu.cn

ABSTRACT

Cell fusion is a widely employed process in various biological procedures, demonstrating significant application value in biotechnology. Cell pairing is a crucial manipulation for cell fusion. Standard fusion techniques, however, often provide poor and random cell contact, leading to low yields. In this study, we present a novel microfluidic device that utilizes a three-path symmetrical channel hydrodynamic capture method to achieve high-efficiency cell capture and pairing. The device contains several symmetrical channels and capture units, enabling three-path capture of two kinds of cells. To better understand the conditions necessary for effective cell pairing, we established a theoretical model of the three-path trapping flow field and conducted a qualitative force analysis on cells. Using K562 cells to explore the effect of different volumetric flow ratios of symmetric channels on cell capture and pairing efficiency, we finally got the optimized structure and obtained a single-cell capture efficiency of approximately 95.6 ± 2.0% and a cell pairing efficiency of approximately 83.3 ± 8.8%. Subsequently, electrofusion experiments were carried out on the paired cells, resulting in a fusion efficiency of approximately 77.8 ± 9.6%.

I. INTRODUCTION

Cell fusion, also known as cell hybridization or somatic cell hybridization, allows two or more homologous or heterologous cells to form hybrid cells asexually *in vitro* through artificial induction and culture processes.[1,2] Cell fusion technology has found widespread applications in various research fields, such as genetics,[3,4] immunomedicine,[5,6] developmental biology,[7] drug or gene transmission,[8,9] cross breeding,[10–12] and others.[13,14] In addition, it demonstrates significant potential in areas like gene regulation, genetic complementarity, gene mapping, and somatic gene recombination.[15–19] Compared with virus/PEG (polyethylene glycol)-induced cell fusion methods, electrofusion has advantages in cell viability, adaptability, and fusion efficiency.

High precision and efficient cell electrofusion involves accurate cell pairing, efficient reversible cell electroporation, stable membrane reconstruction, and cytoplasmic exchange.[20] Cell pairing is a crucial step in the process of cell fusion as it enables the subsequent induction of reversible cell electroporation on the contact cell membrane area between the paired cells.[21] Electrodes are essential components that induce a high-strength electric field for electroporation. Specific shape electrodes or microfluidic channels can generate non-uniform electric

fields to induce dielectrophoretic (DEP) force for effective cell pairing. Due to its improved component adaptability and reduced complexity of microfluidic device, dielectrophoresis-based cell pairing has gained great attention.[22] He *et al.*[23] used long parallel plate gold microelectrode arrays to induce DEP force in capture structure arrays for cell pairing and obtained a pairing efficiency of ∼78%. Kirschbaum *et al.*[24] constructed eight rectangle Pt microelectrodes at the bottom and top of a chip to induce special three-dimensional dielectrophoretic field cages for precise manipulation and pairing of cells. Yoshimura *et al.*[25] reported a device featuring an array of microwells. This device utilizes both the upper ITO (indium tin oxide) electrode and the lower microwell electrode array to induce DEP force in the vertical direction, which is effective for cell pairing. Sakamoto *et al.*[26] designed a microchip with a separating wall containing an array of micro-slits at a regular spacing. Cells can be aligned adjacent to these micro-slits using DEP in a non-uniform electric field. However, solely relying on DEP force may not provide sufficient control over the types and number of cells during the pairing process. This often leads to low-precision and non-target cell pairing, especially for heterologous cell electrofusion.[27] Apart from the above-mentioned dielectrophoresis-based cell pairing

methods, optical,[28] acoustic,[29] and biological[30] based cell manipulation methods have been developed. These methods can precisely manipulate single cells within a microfluidic device, allowing for precise control of desired homo- or heterologous cells. However, the complexity of these operations and their high cost hinder widespread application.

Hydrodynamic cell capture is a purely passive manipulation technique that relies primarily on specific designed microstructures, such as shuttling channel,[31] trigger channel,[32] weir-based trap unit,[33] and cup-shaped structure.[34,35] Both theoretical and simulation analyses indicate that these methods can effectively capture single cells by optimizing parameters such as volumetric flow ratio. Due to its high throughput, accuracy, and efficiency in single-cell capture, hydrodynamic capture is increasingly becoming a preferred solution for single-cell studies[36–38] and biochemical analyses.[39–41] To control the pairing and fusion of two heterologous cells within a microfluidic device, Gel et al.[42] designed a micro-orifice array to separate a microfluidic channel into two independent channels. By using separate inlets, two kinds of cells could be injected into these channels and captured in sequence using hydrodynamic force and dielectrophoresis/gravity force. Skelly et al.[43] used a weir structure to pair cells in three steps. They loaded one kind of cells and directed them to be captured in capture cups by changing their flow trajectory, while the other kind of cells were loaded from the opposite direction to achieve pairing. Meanwhile, van der Berg et al.[44] developed a microfluidic trap array with each trap consisting of a large V-shape trap and a small trap of varying depths. This design enabled the control of B cells and NS-1 cells pairing and fusion. Recently, a microfluidic flip-chip device has been developed to manipulate A549 cells and THP-1 cells through passive hydrodynamic phenomenon and the flipping of the chip.[45] The aforementioned research strongly confirms that the combination of hydrodynamic cell capture methods can significantly enhance cell pairing accuracy, especially when combined with other manipulation methods. However, complex and multi-step manipulation processes could not be avoided.

In this study, a three-path symmetrical channel hydrodynamic capture (SCHC) microfluidic chip was proposed. This design features a specific three-path cell capture structure comprising symmetrical channels and capture units, which allows three-path capture of two kinds of cells. The separate channel and narrow channel between the two traps ensure independent injection of two kinds of cells and accurate pairing and contacting of heterologous cells. Furthermore, the application of electric-field focusing within the narrow channels between the two traps enhances the efficiency of cell fusion. The low volumetric flow ratio characteristic of the three-path channels is particularly beneficial for both cell capture efficiency and cell viability. In addition, the size of a single pairing unit can be reduced, providing a favorable basis for future high-density integration of related structures or enhancing the throughput of single-cell studies and biochemical analyses. To verify the efficiency, accuracy, and convenience of our design, cell pairing and electrofusion experiments using heterozygous fluorescent K562 cells were conducted on this microfluidic chip.

II. RESULTS AND DISCUSSION
A. Mechanism analysis of single-cell capture and cell pairing

The process of cell capture and pairing can be divided into two phases: single-cell capture and single-cell capture in contralateral channel/cell pairing. For the SCHC with a ratio of 100% (see Table S2

for detailed parameters), according to Eqs. (6) and (7), the volumetric flow ratio (VFR) and flow resistance ratio (FRR) between path 1 and path 2 are $Q_1/Q_2 = R_2/R_1 = 9.26$. Similarly, utilizing Eqs. (3) and (8), the VFR and FRR between path 2 and path 3 are $Q_2/Q_3 = R_3/R_2 = 1.35$. Therefore, the FRR of the three paths is $R_1: R_2: R_3 = 1.00: 9.26: 12.50$, while the VFR is $Q_1: Q_2: Q_3 = 1.00: 0.11: 0.08$. Among the three paths, path 1 exhibits the lowest flow resistance and the highest VFR. Therefore, cells will predominantly flow into the traps along the path 1. Subsequently, the presence of cells significantly increases the flow resistance of both path 1 and path 2, rendering path 3 as the path with the lowest flow resistance. The cells will flow along path 3 to the next trap. It is worth noting that a portion of the flow to path 1 is diverted due to the existence of path 2. However, as the flow direction of the cells is toward the traps, this diversion has little effect on single-cell capture (as shown in Fig. S3). Later cells are likely to follow path 3 due to the high flow resistance of other two paths and the absence of extra space to linger near the trap. This can avoid multicellular capture to some extent.

Considering the microstructure geometric parameters and cell size, path 1 and path 2 may become partially obstructed due to captured cells. The flow distributions on these three paths undergo significant changes. On path 1, as shown in Fig. 1(b), the simplified model of the flow channel's geometric parameter undergoes a change after cell capture. Prior to cell capture, the flow channel is a rectangle with length, width, and height of $L = 1\,\mu m$, $W = 7\,\mu m$, and $H = 30\,\mu m$, respectively. After cell capture, the channel is partly clogged, and the height of the rectangular flow channel changes to $H' = 9\,\mu m$ (considering the diameter of K562 cells to be $\sim 21\,\mu m$ under the osmotic pressure of 90 mOsmol kg^{-1}) during cell pairing. The VFR and FRR between path $1'$ and path $2'$ of the contralateral channel are $Q_1'/Q_2' = R_2'/R_1' = 0.32$. Furthermore, the VFR and FRR between path $2'$ and path $3'$ are less affected by the captured cell. We can still obtain $Q_2'/Q_3' = R_3'/R_2' = 1.35$. Furthermore, the VFR and FRR of the three paths are $Q_1': Q_2': Q_3' = 1.00: 3.10: 2.30$ and $R_1': R_2': R_3' = 1.00: 0.32: 0.44$, respectively. This indicates that the VFR of path $1'$ significantly decreases to a minimal level, nearly approaching zero. Consequently, the contralateral channel becomes a traditional single-cell capture structure with two paths. Path $2'$ has the highest VFR, and cells will predominantly follow this path toward the trap in the contralateral channel. In addition, the VFR of path $1'$ is low and almost no fluid flows through it, so it has negligible impact on cell pairing. This could effectively prevent captured cells from being displaced from the desired traps and moved into the contralateral channel.

B. Qualitative force analysis of cells during capture and pairing in combination with simulation

Single-cell movement, capture, and pairing efficiency on microfluidic chip both highly depended on the force condition of cells. Since the path 1 connected the two single cell capture microfluidic channels (path 2 and path 3), it suggested a more intricate flow field and force state of cells, compared with the two individual microfluidic channels. In addition, a force imbalance on path 1 could induce captured cells toward the contralateral channel, potentially causing issues like path blockage, unwanted cell capture, or improper homologous cell pairing. To mitigate the probability of cell moving to the contralateral channel, narrowing the width of path 1 is one approach. However, an equally crucial factor is the control of driving force. The driving force for cell
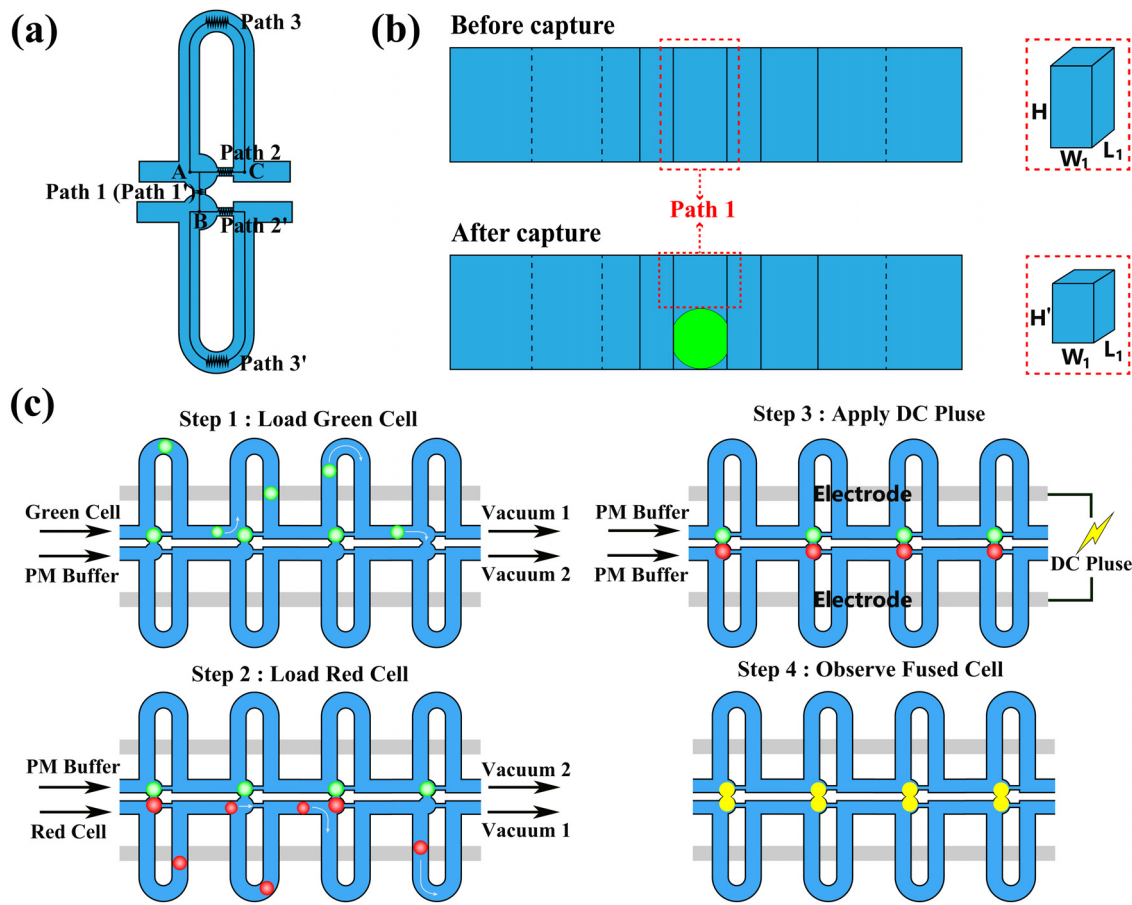
FIG. 1. Theoretical analysis illustration of single-cell capture and cell pairing. (a) Schematic diagram of a single-cell capture unit. (b) Side view of changes in the height of path 1 before and after capturing cell. (c) Four steps for cell pairing and electrofusion.

capture and pairing was generated by negative pressure utilizing the COMSOL Multiphysics 5.6 software for force analysis.

First, when a negative pressure of -0.3 psi and 0 is applied on outlets A and B, respectively, the flow field distribution is shown in Fig. 2(a). The VFR distribution at a trap is mainly concentrated in path 1 and path 2, with a notably higher velocity in the central region of path 1, approximately 200% greater than that of path 2. To simplify and enhance the clarity of the analysis, we focus on the primary dynamics that drive cells toward the trap. The stress model is shown in Fig. 2(d). The fluid within the channel exerts Stokes force F_D on the cell, as given by

$$F_D = 6\pi\eta R\nu, \qquad (1)$$

where η is the viscosity coefficient of the fluid, R is the radius of the cell, and ν is the velocity of the cell relative to the fluid. In simulation analysis, cells are assumed to move with low Reynolds number ($Re \ll 1$) within a homogeneous viscous fluid (η is a constant value) with no change in morphology. Therefore, the magnitude of F_D is only related to ν. Cells are subjected to Stokes forces, F_{D1} and F_{D2}, along the X and Y axes, respectively. These two Stokes forces drag the cells toward the traps. However, due to the strong elasticity of the cell membrane, the cell is prone to being squeezed and deformed by the strong action of F_{D1}, allowing it to pass through path 1. To reduce F_{D1}, an unequal negative pressure of -0.1 to -0.3 psi [negative pressure 2, Fig. 2(e)] was applied to the contralateral channel. This resulted in a significant decrease in the velocity of path 1 from 3.34×10^{-4} to 2.34×10^{-4} m s^{-1} [Fig. 2(b)], while there was a slight increase in the velocity of path 2 from 1.69×10^{-4} to 1.98×10^{-4} m s^{-1}. The force analysis result is depicted in Fig. 2(e). In the X-axis direction, the cell changes from being subjected only one Stokes force, F_{D1}, to being influenced by two Stokes forces, F'_{D1} and F'_{D3}, generated by the fluid in the symmetrical channels on both sides. In addition, the cell are also subjected to a Stokes force, F'_{D2}, in the Y-axis direction; however, F'_{D2} is about 1.2 times greater than F_{D2}. The flow velocities in the central area of path 1 and path 2 are about 2.34×10^{-4} m s^{-1} and 1.98×10^{-4} m s^{-1}, respectively. Consequently, the resultant force F_D comprising F'_{D1} and F'_{D3} is approximately 1.2 times greater than F'_{D2}. Despite this, the VFR in path 1 is higher than in path 2 due to the larger cross-sectional area of path 1. Compared to the one-sided negative pressure application, F_D is approximately twice smaller than F_{D1}. Under the
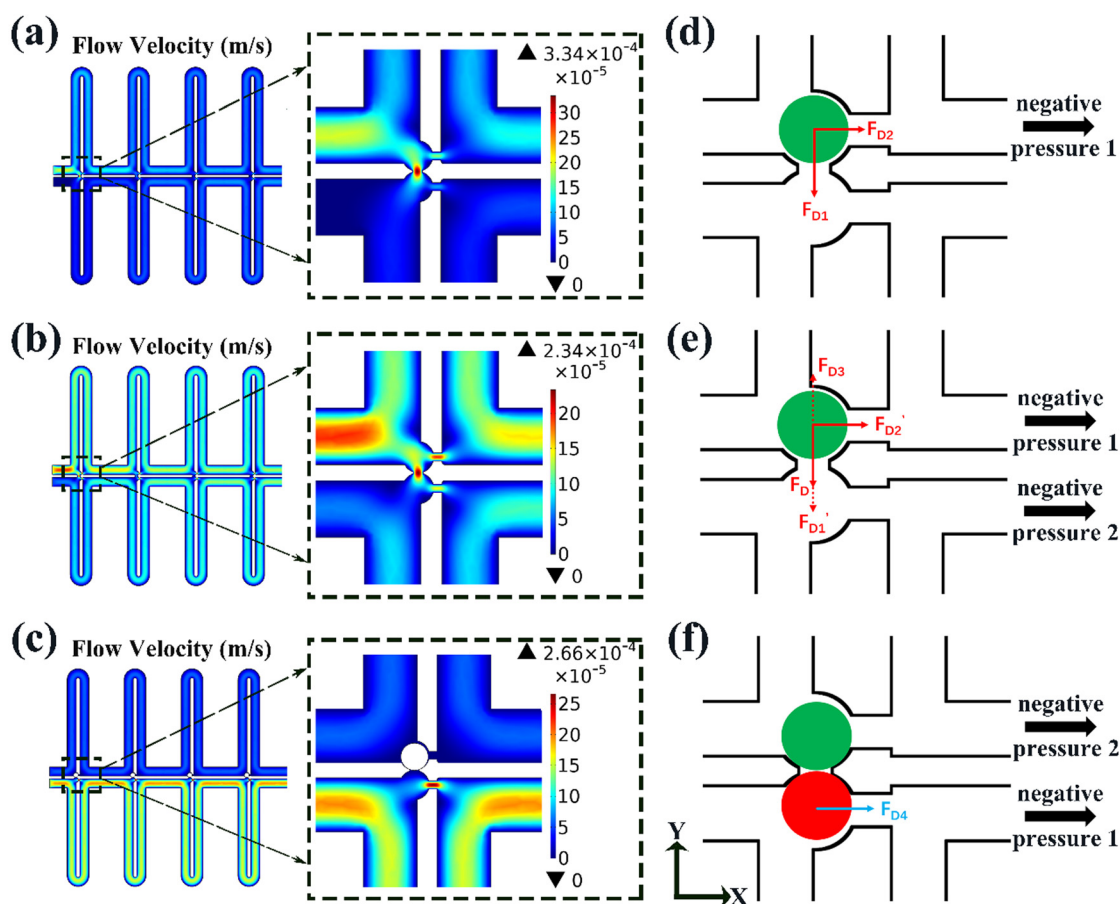
FIG. 2. Flow field and qualitative analysis of the force on cells in the process of single-cell capture and cell pairing. (a) Flow velocity in the symmetrical channel when vacuum is applied unilaterally in the designed capture microstructure simulated by COMSOL. (b) Flow velocity in the symmetrical channel when vacuum is applied on both sides in the designed capture microstructure simulated by COMSOL. (c) Simulation of flow velocity on the other side of the symmetrical channel after one side captures the cells. (d) Schematic diagram of the forces subjected to cells in the channel when vacuum was applied on outlet A. (e) Schematic diagram of the forces subjected to cells in the channel when vacuum was applied on outlet A and outlet B. (f) Schematic diagram of the forces subjected to cells in the channel during cell pairing.

combined action of F_D and F'_{D2}, cells will be captured, greatly reducing the possibility of crossing path 1 due to the reverse effect of F_{D3}.

Since the channel on the side of the captured cell no longer needs a large negative pressure to provide the driving force for capture, the intensities of negative pressure at the outlets are exchanged. The reduced negative pressure enhances the stability of the captured cells and mitigates any potential influence on cell activity resulting from high fluid shear force. Figure 2(c) illustrates the flow field distribution after cells have been trapped within the unilateral channel. Following cell capture, the flow is concentrated in path 3, with negligible flow field distribution along path 1 due to the existence of the cell. Consequently, the flow velocity in the central area of path 1 (path 1′) is 1.11×10^{-6} m s^{-1}. The fastest flow velocity is observed at the center of path 2′ in the contralateral channel, reaching 2.66×10^{-4} m s^{-1}, which is 240 times faster than that of path 1′. Therefore, the captured cell is mainly subjected to a Stokes force, F_{D4}, along the Y-axis direction, which induces cell movement toward the trap to complete the pairing process. The force acting on the cell near the symmetrical channels trap is shown in Fig. 2(f).

C. Effect of different volumetric flow ratios in symmetric channels on cell capture and pairing efficiency

To prevent cells from passing through path 1, the channel parameters of path 1 were first determined within a certain range based on the typical diameter of mammalian somatic cells (10–30 μm). However, while ensuring that path 1 remains the path with the lowest flow resistance, variations in VFRs of path 2 and path 3 in symmetrical channels also have a significant impact on the efficiency of cell capture and pairing.

According to Pendharkar et al.,[46] a conventional two-path hydrodynamic microfluidic chip with a VFR of $Q_2/Q_3 = 1.35$ demonstrates the highest single-cell capture efficiency. To investigate the influence of VFR on single-cell capture and optimize the geometry of the single-cell capture unit, a series of microfluidic chips with different VFR values were designed and fabricated (detailed parameter information is presented in Table S2). The experimental results for single-cell capture and cell pairing reflected variations in efficiency

across a range of VFR values from 0.68 to 3.75. It can be observed that as the VFR increased from 0.68 to 2.03, the efficiency of single-cell capture and cell pairing also increased. Specifically, when the VFR was equal to 2.03, both the single-cell capture efficiency and cell pairing efficiency reached their peak values of 95.6 ± 2.0% and 83.3 ± 8.8%, respectively. However, an increase in the VFR from 2.03 to 3.75 resulted in a decrease in the efficiency of single-cell capture and cell pairing [as shown in Fig. 3(e)].

According to the theory established by Tan,[47] when the VFR is 1 or below, it is difficult to capture cells successfully for conventional two-path hydrodynamic structures. However, when the VFR exceeds 1, the ability to trap cells improves. In the SCHC, the three-path design
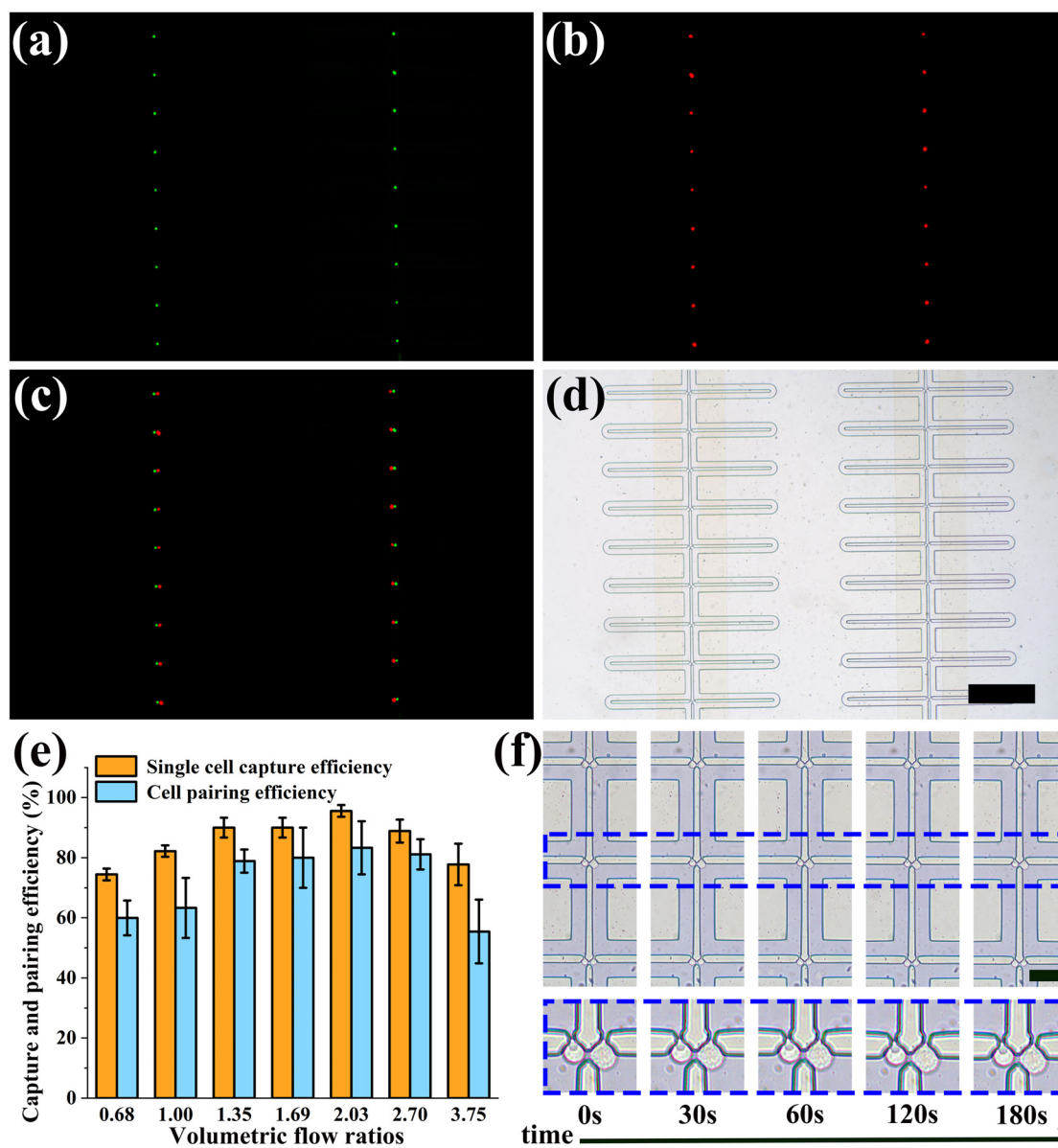

FIG. 3. Single-cell capture and cell pairing in the microfluidic device. (a) Green fluorescence image of K562 cells in microfluidic device channels after single cell capture. (b) Red fluorescence image of K562 cells in microfluidic device channels after cell pairing. (c) Red and green fluorescence overlay image of K562 cells paired in the device. (d) Image of K562 cells paired in the device under bright field. (e) Comparison of single cell capture efficiencies (the percentage of traps occupied by one green cell) and cell pairing efficiencies (the percentage of pairing units occupied by one green cell and one red cell) of the microfluidic device with different volumetric flow ratios. The results were presented as mean ± standard deviation (n = 3). (f) Time course of trypan blue staining of paired K562 cells in the microfluidic device. Inside the blue dotted line is a detailed view of a pair of cells. Scale bar: 500 μm.

enabled successful single-cell capture with a VFR range of 0.68 to 1, achieving average efficiencies of 74.4% ± 2.0% and 82.2 ± 1.9%, respectively. A lower VFR indicates the reduced area required for each capture unit, or the integration of more capture units onto the microfluidic chip with the same area (Table S3). This demonstrates significant potential for high-throughput cell screening, single cell co-culture, and other applications. When the VFR was greater than 1, there was a steady increase in the efficiency for both single-cell capture and cell pairing. However, a decline in capture and pairing efficiency was observed when the VFR exceeded 2.03. It could be induced by increasing the VFR of path 2 and path 3, which caused a further reduction in the flow division through path 3. Additionally, high velocity around the trap would also be induced by the increasing flow in path 1 and path 2. These two factors would enhance the single-cell capture efficiency of SCHC. Moreover, the flow in path 2′, which became the main pathway for B cell capture during the pairing process, would also increase due to the increase in VFR. From the theory established by Tan,[47] when the VFR is bigger than 1 and exceeds a certain value, multiple-cell capture may occur within the traps. Similarly, when the VFR of SCHC exceeds 2.03, multiple cells may also be captured at the same trap site. As the flow in path 1 continues to increase as VFR increases from 2.03, cells may either pass through the trap or accumulate around it, leading to a decrease in single-cell capture and cell pairing efficiency. In addition, the length of the channel will increase with the increasing VFR. The treatment time increasing in high flow velocity condition, could result in a potential risk to cellular activity. Thus, $Q_2/Q_3 = 2.03$ is a favorable value for single-cell capture and cell pairing on the SCHC in this study.

D. Cell pairing and activity assay

Based on the optimization of VFR in SCHC, a symmetric channel design with a Q_2/Q_3 ratio of 2.03 was developed. To validate the performance of the optimized device, K562 cells marked with CMFDA (green) and CMTPX (red) were used to conduct the experimental research. By applying a consistent negative pressure of −0.3 psi to outlets A and B, the CMFDA-labeled K562 cells were efficiently captured in the traps of SCHC. Subsequently, the CMTPX-labeled cells were loaded into the microfluidic chip and captured as individual cells. In both bright and dark fields, it can be seen that green cells and red cells were closely one-to-one contacted through path 1 [as shown in Figs. 3(a)–3(d) and S4]. Remarkably, high cell pairing efficiency [up to 93.3% Fig. 3(e)] was achieved, which provided a favorable condition for following cell electrofusion.[48]

Moreover, given the potential risk of high flow velocity conditions to cellular activity, the survival rate of cell was evaluated using trypan blue staining. A 0.4% trypan blue solution was injected into the microfluidic chip immediately after completing the cell pairing process. We observed the staining of paired cells within 3 min to analyze the effect of the pairing process on cell activity. The results [Figs. 3(f) and S5] indicated that the paired cells exhibited distinct cell morphology, remaining colorless or translucent while maintaining close contact from 0 to 3 min post-injection of trypan blue solution. A survival rate of up to 95.8 ± 3.9% (n = 3) was obtained for paired cells during the cell pairing process of SCHC. Flow field in the device after cell pairing was also simulated. The cells outside the trap were then taken as the sampling site, and the fluid shear stress on

these sites was calculated (Fig. S6). The maximum shear stress of the cells was about 0.5 Pa, which was insufficient to cause significant damage to the viability of cells.[49] This demonstrates that our device preserves cellular activity for a certain duration after cell capture and pairing, thereby not interfering with subsequent cell electrofusion operations.

E. Cell electrofusion in the microfluidic device

To further assess the feasibility of applying the device to cell electrofusion, we used COMSOL software to simulate and analyze cell electroporation during the electrofusion process. Figure 4(a) presents the simulation result of electric field intensity in the microfluidic chip, specifically around the paired cells under experimental voltage and electrode parameters. It reveals that the electric field is focused in the cell contact area, while other parts of the chip exhibit weaker fields. Path 1 can optimize the electric field distribution within the chip, inducing a localized high electric field in the connection area. The electric field intensity at the center of the contact area approximately ranges from 4 to 5 kV/cm, which is within the suitable range for inducing reversible electroporation. Figures 4(b)–4(d) illustrate the distribution of transmembrane voltage (TMV), pore density, and pore radius of electroporation on the paired cell membrane. Based on the TMV distribution, we selected five points with higher TMV on the cell membrane to analyze their trends in TMV, pore density, and pore radius over a 10 μs period. Figure 4(b) shows that the TMV at the contact point and points 1–4 (P_1–P_4) increases with time. The TMV at the contact point exceeds 1 V within 10 μs, which is regarded as cell electroporation.[50,51] In contrast, the TMV at P_1–P_4 is consistently less than 0.6 V. Within the 10 μs duration, the pore density at the contact point increases exponentially and then stabilizes. The pore density values at P_1–P_4 remain approximately on the order of 10^9. Specifically, the pore density at the connect point is 1.63×10^{13} m^{-2}, while the maximum pore density around P_1–P_4 is only approximately 1.31×10^8, 1.81×10^9, 5.86×10^{11}, and 6.53×10^{11} m^{-2}, respectively. The pore density at the contact point is significantly larger by two to five orders of magnitude compared to the pores around P_1 to P_4. In addition to the high pore density, the contact areas predominantly consist of large pores with a radius ranging from approximately 50 to 60 nm. In contrast, the pores near P_1–P_4 are small, having a pore radius of only 10–20 nm. The pore radius around 60 nm is sufficiently large to promote cell fusion, whereas pores smaller than 20 nm are not conducive to cell fusion.[51] This result may indicate that during the fusion process of paired cells perforated and fused in the contact area, there is no perforation in other areas. Therefore, the structure of the SCHC optimizes the electric field, enabling the paired cells to induce large and dense pores only in the contact area, thereby promoting efficient cell electrofusion.

After the cell pairing process, the fusion process was initiated through the electric pulse application. Movie S1 shows the fusion process of the paired cells in our device, exhibiting a clear phenomenon of cell fusion observable within 3 min [Fig. 4(e)]. Figures 4(f)–4(m) present a comparison of the bright field and dark field images before and after the fusion of the paired cells. Two kinds of paired cells can exhibit green or red fluorescence under the same excitation light after fusion [Figs. 4(k) and 4(l)], whereas before fusion, each cell only displayed one kind of fluorescence under a single excitation light. The contact area between the cells demonstrated yellow fluorescence in the dark
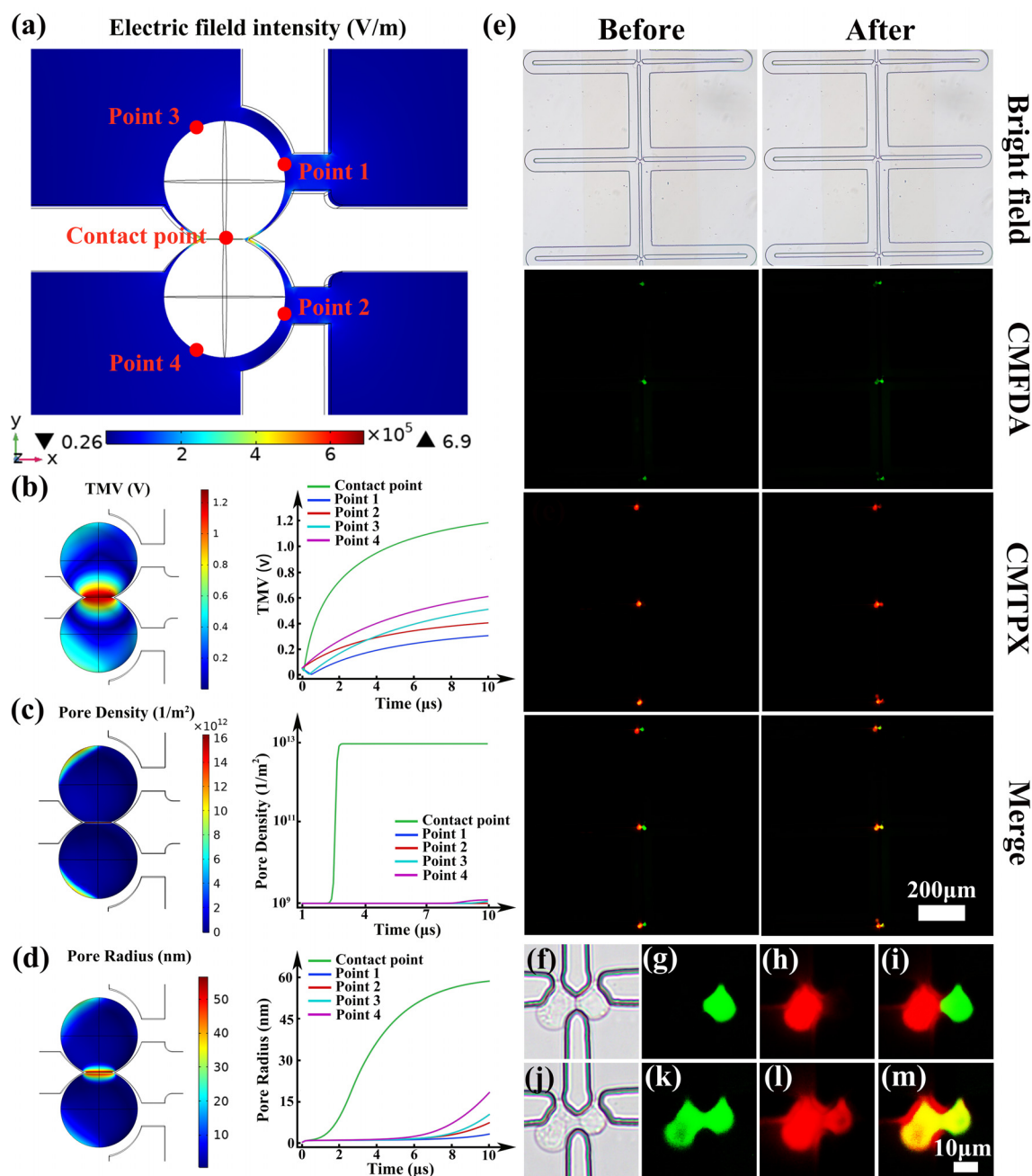
FIG. 4. Cell electrofusion in the microfluidic device. (a) Electric field intensity in symmetrical channels around paired cells simulated by COMSOL. (b)–(d) Simulation results and transient change curve of TMV, pore density, and pore radius of the paired cells in 10 μs. The contact point is the central point of the cell–cell interface. Point 1 is the intersection point of a line that forms a 15° angle with the radius of the cell shown in Fig. 4(a). Point 2 is the point symmetric to point 1 about the cell–cell interface. Point 3 and point 4 are the maximum value of TMV at the distal end of the cells. (e) Image of K562 cells under bright field and fluorescence field before and after cell electrofusion. (f) Image of K562 cells under bright field and with (g) green fluorescence, (h) red fluorescence, and (i) fluorescent overlay before cell electrofusion. (j) Image of K562 cells under bright field and with (k) green fluorescence, (l) red fluorescence, and (m) fluorescent overlay after cell electrofusion.

field [Fig. 4(m)], indicating a cytoplasmic exchange between the cells and successful transfer of the fluorescent dye to a different cell during fusion. Comparing Figs. 4(f) and 4(j), it can be observed that the membrane boundary between the paired cells disappeared after fusion.

Within approximately 30 min, the reorganization of the cell membrane was completed, resulting in the formation of heterozygous cells. Subsequently, we pushed the fused heterozygous cells out of the structure by applying a positive pressure (Movie S2), revealing a complete

spherical shape of the cells. Ultimately, a fusion efficiency of approximately $77.8 \pm 9.6\%$ ($n = 3$) have been obtained for SCHC device (Movie S3).

III. CONCLUSION

In this study, we proposed a new hydrodynamic heterologous cell pairing method. By employing the design of a three-path symmetrical channel in the microfluidic chip, we significantly enhanced cell capture and pairing efficiency in comparison with traditional two-path hydrodynamic-based structures. Consequently, we achieved a single-cell capture efficiency of $\sim\!95.6 \pm 2.0\%$ and a pairing efficiency of $\sim\!83.3 \pm 8.8\%$ (Table S4). Electrofusion experiments were carried out on the paired cells, achieving a fusion efficiency of $\sim\!77.8 \pm 9.6\%$. This proposed method of cell capture and pairing is purely passive and has little damage to cells compared to other active methods. Furthermore, SCHC device allows the flow velocity required for cell capture to be kept at a low level, thereby minimizing shear-induced cell damage. More importantly, SCHC device enables the chip to capture cells at low VFRs (<1), facilitating high throughput and high-density integration. However, since the proximity of cell sizes involved in this study, the device designed in this work may encounter challenges when dealing with heterologous cells with significant size differences, which will be improved in the future. We believe that our device and accurate pairing method will hold great potential for applications in various fields, including single-cell analysis, cell co-culture, exocrine research, and others.

IV. METHODS

A. Device design

To ensure high through-put and accurate heterologous cell pairing, a microfluidic chip was developed consisting of 50 SCHC cell capture and pairing units [Figs. 5(a) and 5(b)]. Each SCHC unit [Fig. 5(c)] is comprised of sinusoidal-wave-shaped loop channels (path 3) stacked on a straight channel (path 2). These straight channels possess narrowed regions that serve as traps. The traps were set to $22\,\mu m$ to ensure that most of mammalian somatic cells can be captured. The parameters L_1–L_3 and W_1–W_3 of the microchannel in Fig. 5(a) represent the lengths and widths of paths 1, 2, and 3, respectively. The height of the microchannel H was set to $30\,\mu m$. Two symmetrical cell traps are connected by a vertical channel (path 1) to regulate the flow field. The design of the channels ensures that when a trap is empty, path 1 has a lower flow resistance than both paths 2 and 3. This results in a majority of the fluid flowing along path 1. Cells in the flow are carried by this main stream into the traps, where they serve as plugs, significantly increasing the flow resistance along both path 1 and path 2. This redirects the main flow into path 3. Subsequently, other cells will flow along path 3, bypassing the already filled traps. The symmetric channel employs a similar principle to transport the other type of cell to the traps, with both types of cells being paired and in contact via
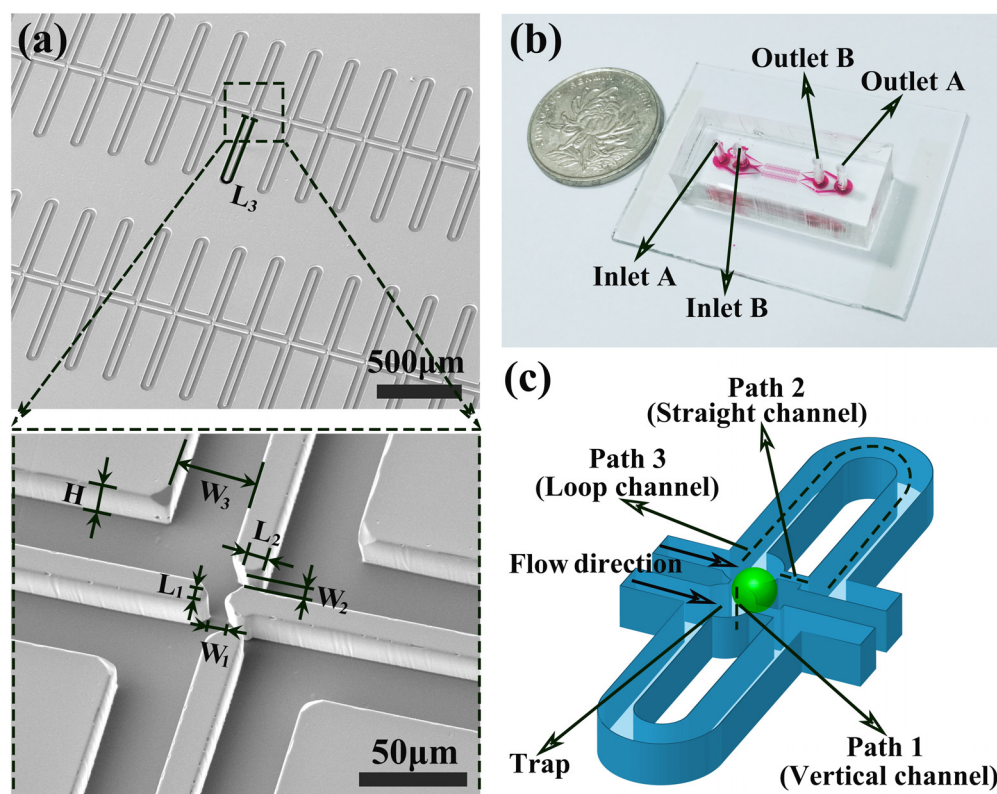

FIG. 5. Structure of microfluidic device. (a) Scanning electron micrograph images of the device detailing the trap structure. (b) Image of the microfluidic device bonded to an ITO glass slide patterned with electrodes. Red ink is filled to visualize the device structure. (c) Three-dimensional schematic diagram of a pairing unit.

path 1. The electrodes were designed as an interdigital array, with each pair arranged in parallel on both sides of a row of pairing units. The electrode length was set to 38 mm, and the electrode width was 200 μm. The distance between electrodes was 80 μm to balance the field strength and the alignment process of the chips and electrodes (Fig. S1). After an electric signal is applied, a non-uniform electric field is generated between the electrodes, focused inside the traps with the highest electric field strength occurring near the tip structure.

B. Device fabrication

The microfluidic chip was fabricated by standard soft photolithography techniques and polydimethylsiloxane (PDMS) molding. A 30-μm thick SU-8 mold was fabricated by photolithography, including steps like lithography, development, curing, and post-treatment. The PDMS (Sylgard 184, Dow Corning, Midland, MI, USA) was poured into the SU-8 mold for casting. Meanwhile, indium tin oxide (ITO) electrodes for cell electroporation were prepared through a sequence of processes including lithography, development, wet etching, and masking layer removing. Finally, the PDMS and ITO electrodes were irreversibly bonded together through plasma treatment. A detailed fabrication process is shown in Fig. S2.

C. Theory for three-path symmetrical channel

Considering the symmetrical geometric configuration of the SCHC, the flow resistance within channels on both sides is identical, making the analysis of flow resistance on both sides equivalent.

Using the Darcy–Weisbach equation to determine pressure drop or pressure difference in a unilateral microchannel of the SCHC and solving the continuity and momentum equations for the Hagen–Poiseuille flow problem, we can derive the pressure difference as

$$\Delta p = \frac{C(\alpha)}{32} \cdot \frac{\mu L Q P^2}{A^3}, \qquad (2)$$

where $C(\alpha)$ is a constant related to the aspect ratio $(0 < \alpha < 1)$, μ is the fluidic viscosity, L is the length of the channel, Q is the volumetric flow rate, and A and P are the cross-sectional area and perimeter of the channel, respectively. For a rectangular channel, the relationships $A = W \times H$ and $P = 2(W + H)$ are employed, where W and H are the width and height of the channels respectively.

Fluid can flow from junction A to B via path 1 or flow from A to C via path 2 or 3 (with analogous paths in the contralateral channel labeled as path 1′, path 2′, and path 3′) as shown in Figs. 1(a) and 1(b). Cells in the flow will be carried by main stream into the trap during trapping. Ignoring the small losses caused by bending, widening/narrowing, etc., Eq. (2) is applied separately to paths 2 and 3. Since the pressure drop is the same for both paths (junction A to C), we can equate the expressions to obtain

$$\frac{Q_2}{Q_3} = \left(\frac{C_3(\alpha_3)}{C_2(\alpha_2)}\right) \cdot \left(\frac{L_3}{L_2}\right) \cdot \left(\frac{W_3 + H}{W_2 + H}\right)^2 \cdot \left(\frac{W_2}{W_3}\right)^3, \qquad (3)$$

where the subscripts 2 and 3 denote paths 2 and 3, respectively. The pressure drop of path 1 (junction A to B) is different from the other two paths. Therefore, the volumetric flow ratio cannot be directly obtained by using Eq. (3). So we introduced others equations to establish a connection among them.

In fluids, Poiseuille's law can be used to obtain the resistance equation,

$$R = \frac{\Delta p}{Q}. \qquad (4)$$

By combining Eqs. (2) and (4), the fluid resistance of the channel can be simplified as

$$R = \frac{C(\alpha)}{32} \mu L \frac{4(W + H)^2}{(WH)^3}. \qquad (5)$$

Here, using Eq. (5), the flow resistance of path 1 and path 2 was calculated, respectively, and then, we arrive at

$$\frac{R_2}{R_1} = \left(\frac{C_2(\alpha_2)}{C_1(\alpha_1)}\right) \cdot \left(\frac{L_2}{L_1}\right) \cdot \left(\frac{W_2 + H}{W_1 + H}\right)^2 \cdot \left(\frac{W_1}{W_2}\right)^3. \qquad (6)$$

Comparing Eqs. (3) with (6), we can easily obtain

$$\frac{Q_1}{Q_2} = \frac{R_2}{R_1} \qquad (7)$$

and

$$\frac{Q_2}{Q_3} = \frac{R_3}{R_2}. \qquad (8)$$

In this way, the volumetric flow ratio and flow resistance ratio of the three paths establish a connection with each other.

D. Cell culture and preparations

To assess the performance of one-step single-cell capture, heterologous cell pairing, and electrofusion on the SCHC microfluidic chip, human leukemia K562 cells were used in experimental research. K562 cells were cultured in an incubator (Forma 381, Thermo Scientific, USA) maintained at 37 °C in 5% CO$_2$ and were passaged twice a week using Roswell Park Memorial Institute (RPMI) 1640 medium supplemented with 10% fetal bovine serum (FBS, Gibco, USA) and 1% penicillin–streptomycin (Biosharp, China). In addition, to simplify the experimental procedure and clearly demonstrate the ability of heterologous cell manipulation, K562 cells were stained with green and red fluorescent dyes using CellTracker™ Green (CMFDA) and CellTracker™ Red (CMTPX), respectively. Cells are harvested by centrifugation, with the supernatant subsequently aspirated. They are then gently resuspended in pre-warmed CellTracker™ working solution and incubated for 25 min at a temperature of 37 °C. The stained cells were then centrifuged at 300 g for 5 min to obtain the cell precipitates. A pulsing medium buffer solution (PM buffer) with an electric conductivity of 53 mS m^{-1} and an osmolality of 90 mOsmol kg^{-1} was prepared with a hypotonic buffer containing 0.1 mM CaCl$_2$, 0.1 mM MgCl$_2$, and 90 mM sorbitol. This buffer was used to resuspend the cells and obtain the cell suspension for conducting the experiments.

E. Device working procedure

In order to prevent cell adhesion to the microchannel wall of the SCHC device, it is initially conditioned for about 15 min with a 1% dilution of bovine serum albumin (BSA) in ultrapure water. A microfluidic pressure controller (PG-MFC-8CH, PreciGenome, USA) was used to apply a negative pressure. The cell pairing working procedure of the SCHC device involves the following four steps [Fig. 1(c)]: (1) A 10 μL

suspension of green fluorescence K562 cells suspension is loaded from inlet A by applying a negative pressure (-0.3 psi) at outlet A. Concurrently, $10 \mu L$ of PM buffer is loaded from inlet B by applying a negative pressure (-0.1 psi) at outlet B. After most of the traps are filled with cells, an additional $10 \mu L$ of PM buffer is loaded to wash away uncaptured cells within the channel. (2) With the negative pressure of outlet A and outlet B exchanged, a suspension of red fluorescence K562 cells is loaded from inlet B. A cleaning step with PM buffer is performed similarly to step 1 when most of the traps are filled. When a single green cell is paired with a single red cell in SCHC units, it is defined as a successful pairing. (3) During the process of electrofusion, the same negative pressure (-0.1 psi) is applied at both outlets to keep paired cells in close contact. A DC pulse (V_{pp}: 15 V, duration: 10 μs, and the number of pulses: 5) is applied by a cell electrofusion machine (BEX, Japan) to induce reversible electroporation in the cell membrane. Immediately after, a promote fusion signal (essentially an attenuated sinusoidal signal) is applied to promote membrane connection and remodeling between the two cells during electrofusion. (4) Clear cell fusion phenomenon can be observed within 3 min. Fusion images were obtained using an inverted microscope (IX73, Olympus, Tokyo, Japan) with an attached Orca-ER CCD device (IMG, China) and control software. Images of fused and unfused cells were taken before and after the application of electrical signals to paired cells under bright field and dark field, respectively.

F. Cell activity assay

0.4% trypan blue solution was injected into the microfluidic chip channels at the end of cell pairing and cell electrofusion. The assessment of cell viability was carried out by analyzing the percentage of unstained cells, providing a metric to quantifiably evaluate the effects of the manipulation procedure on cell activity.

G. COMSOL simulation

Numerical simulation was performed using COMSOL (COMSOL Multiphysics 5.6, Stockholm, Sweden). The Navier–Stokes equations were used for the calculations involved in fluid dynamics. An electroporation model was established to calculate the transmembrane voltage (TMV).[20] The AC/DC module was used to determine the electric field distribution in the microchannel. The boundary condition of simulation is shown in the supplementary material. A detailed description of the model parameters can be found in Table S1.

SUPPLEMENTARY MATERIAL

See the supplementary material for additional information on parameters of the electrode (Fig. S1); fabrication details of the microfluidic device (Fig. S2); schematic diagram of the forces on cell during cell capture (Fig. S3); boundary condition of simulation; constants, and parameter values used in the simulation (Table S1); geometric dimensions of microchannel (Table S2); paired K562 cells in different microfluidic devices (Fig. S4); the area of a single pairing unit of symmetrical channel with different values of Q_1/Q_2 (Table S3); trypan blue staining image (Fig. S5); fluid shear stress of paired cells (Fig. S6); comparative analysis with previously reported works (Table S4); and finally, three supplementary movies included, to show the details of cell electrofusion (Movie S1), the process of pushing fused cells out of the chip (Movie S2), and a zoom-out video of cell fusion in the device (Movie S3), respectively.

AUTHOR DECLARATIONS

Conflict of Interest

The authors have no conflicts to disclose.

Ethics Approval

Ethics approval was not required.

Author Contributions

Xuefeng Wang: Formal analysis (lead); Investigation (lead); Methodology (lead); Validation (lead); Writing – original draft (lead). **Yaqi Bai:** Investigation (supporting). **Xiaoling Zhang:** Investigation (supporting); Writing – review & editing (supporting). **Wei Li:** Investigation (supporting). **Jun Yang:** Funding acquisition (equal); Supervision (equal). **Ning Hu:** Conceptualization (lead); Funding acquisition (equal); Supervision (equal); Writing – review & editing (lead).

DATA AVAILABILITY

The data that support the findings of this study are available from the corresponding author upon reasonable request.

REFERENCES

[1] E. H. Chen and E. N. Olson, Science **308**, 369–373 (2005).
[2] B. M. Ogle, M. Cascalho, and J. L. Platt, Nat. Rev. Mol. Cell Biol. **6**, 567–575 (2005).
[3] J. H. T. Song, R. L. Grant, and V. C. Behrens, Proc. Natl. Acad. Sci. **118**, e2117557118 (2021).
[4] J. M. Melancon, T. P. Foster, and K. G. Kousoulas, J. Virol. **78**, 7329–7343 (2004).
[5] T. Minowa, Y. Hirohashi, K. Murata, K. Sasaki, T. Handa, M. Nakatsugawa, Y. Mizue, A. Murai, T. Kubo, T. Kanaseki, T. Tsukahara, S. Iwabuchi, S. Hashimoto, A. Ishida-Yamamoto, H. Uhara, and T. Torigoe, J. Pathol. **260**, 304–316 (2023).
[6] Y. Tajima, F. Shibasaki, and H. Masai, Cancer Gene Ther. **31**, 158–173 (2024).
[7] D. M. Lee and E. H. Chen, Annu. Rev. Genet. **53**, 67–91 (2019).
[8] F. Sadeghian, S. Hosseinkhani, A. Alizadeh, and A. Hatefi, Int. J. Pharm. **427**, 393–399 (2012).
[9] M. Ušaj, M. Pavlin, and M. Kandušer, J. Membr. Biol **257**, 377–389 (2024).
[10] M.-S. Hung, Y.-M. Zhao, K. O. Okeyo, and O. Kurosawa, BioNanoScience **14**, 4520–4531 (2024).
[11] R. Jahn, T. Lang, and T. C. Südhof, Cell **112**, 519–533 (2003).
[12] K. Sala-Cholewa, A. Milewska-Hendel, R. Pérez-Pérez, E. Grzebelus, and A. Betekhtin, Plant Cell, Tissue Organ Cult. **157**, 26 (2024).
[13] S. Takamori, P. Cicuta, S. Takeuchi, and L. D. Michele, Nanoscale **14**, 14255–14267 (2022).
[14] W. Wu, Y. Qu, N. Hu, Y. Zeng, J. Yang, H. Xu, and Q. Zheng, PLoS One **10**, e0131966 (2015).
[15] D. J. Ambrosi, B. Tanasijevic, A. Kaur, C. Obergfell, R. J. O'Neill, W. Krueger, and T. P. Rasmussen, Stem Cells **25**, 1104–1113 (2007).
[16] M. Tada, Y. Takahama, K. Abe, N. Nakatsuji, and T. Tada, Curr. Biol. **11**, 1553–1558 (2001).
[17] S. M. Daniel, P. Raipuria, and B. C. Sarkhel, Small Ruminant Res. **77**, 45–50 (2008).
[18] P. Qu, C. Shen, Y. Du, H. Qin, S. Luo, S. Fu, Y. Dong, S. Guo, F. Hu, Y. Xue, and E. Liu, Sci. Rep. **10**, 2186 (2020).

[19]M. Kato, E. Sasamori, T. Chiba, and Y. Hanyu, J. Immunol. Methods **373**, 102–110 (2011).

[20]X. Zhang, N. Hu, X. Chen, T. Fan, and S. Qian, Sens. Actuators, B **240**, 434–442 (2017).

[21]N. Hu, J. Yang, S. W. Joo, A. N. Banerjee, and S. Qian, Sens. Actuators, B **178**, 63–85 (2013).

[22]M. Sen, K. Ino, J. Ramón-Azcón, H. Shikua, and T. Matsue, Lab Chip **13**, 3650–3652 (2013).

[23]W. He, L. Huang, Y. Feng, F. Liang, W. Ding, and W. Wang, Biomicrofluidics **13**, 054109 (2019).

[24]M. Kirschbaum, C. R. Guernth-Marschner, S. Cherré, A. de Pablo Peña, M. S. Jaeger, R. A. Kroczek, T. Schnelle, T. Mueller, and C. Duschl, Lab Chip **12**, 443–450 (2012).

[25]Y. Yoshimura, M. Tomita, F. Mizutani, and T. Yasukawa, Anal. Chem. **86**, 6818–6822 (2014).

[26]S. Sakamoto, K. O. Okeyo, S. Yamazaki, O. Kurosawa, H. Oana, H. Kotera, and M. Washizu, Biomicrofluidics **10**, 054122 (2016).

[27]F. S. Hamdi, O. Français, F. Subra, E. Dufour-Gergam, and B. Le Pioufle, Biomicrofluidics **7**, 44101 (2013).

[28]Y.-C. Hsiao, C.-H. Wang, W.-B. Lee, and G.-B. Lee, Biomicrofluidics **12**, 034108 (2018).

[29]X. Liu, W. Zhang, U. Farooq, N. Rong, J. Shi, N. Pang, L. Xu, L. Niu, and L. Meng, Lab Chip **22**, 921–927 (2022).

[30]A. Desalvo, F. Bateman, E. James, H. Morgan, and T. Elliott, Lab Chip **20**, 3772–3783 (2020).

[31]C.-K. He, Y.-W. Cheng, S.-H. Wang, and C.-H. Hsu, Lab Chip **19**, 1370–1377 (2019).

[32]H. Chai, Y. Feng, F. Liang, and W. Wang, Lab Chip **21**, 2486–2494 (2021).

[33]B. Dura, Y. Liu, and J. Voldman, Lab Chip **14**, 2783–2790 (2014).

[34]D. Lv, X. Zhang, M. Xu, W. Cao, X. Liu, J. Deng, J. Yang, and N. Hu, Electrophoresis **43**, 2165–2174 (2022).

[35]J. Kim, J. Erath, A. Rodriguez, and C. Yang, Lab Chip **14**, 2480–2490 (2014).

[36]L. Li, H. Wang, L. Huang, S. A. Michael, W. Huang, and H. Wu, Anal. Chem. **91**, 15908–15914 (2019).

[37]W. Shi, J. Qin, N. Ye, and B. Lin, Lab Chip **8**, 1432–1435 (2008).

[38]Y. Cai, E. Yu, J. Jin, Y. Liu, and H. Chen, Lab Chip **23**, 3467–3478 (2023).

[39]M. Tayebi, Y. Zhou, P. Tripathi, R. Chandramohanadas, and Y. Ai, Anal. Chem. **92**, 10733–10742 (2020).

[40]F. A. Shaik, C. Lewuillon, B. Ahmadian, C. Brinster, A. Guillemette, B. Quesnel, Y. Touil, L. Lemonnier, and M. C. Tarhan, Lab Chip **22**, 908–920 (2022).

[41]Q. Mou, Y. Bai, M. Xu, D. Lv, J. Deng, N. Hu, and J. Yang, Anal. Chem. **95**, 8533–8540 (2023).

[42]M. Gel, Y. Kimura, O. Kurosawa, H. Oana, H. Kotera, and M. Washizu, Biomicrofluidics **4**, 022808 (2010).

[43]A. M. Skelley, O. Kirak, H. Suh, R. Jaenisch, and J. Voldman, Nat. Methods **6**, 147–152 (2009).

[44]E. W. M. Kemna, F. Wolbers, I. Vermes, and A. van den Berg, Electrophoresis **32**, 3138–3146 (2011).

[45]G. Pendharkar, Y.-T. Lu, C.-M. Chang, M.-P. Lu, C.-H. Lu, C.-C. Chen, and C.-H. Liu, Cells **10**, 2855 (2021).

[46]Y. Bai, X. Zhang, X. Wang, M. Xu, J. Yang, and N. Hu, Anal. Chem. **96**, 4437–4445 (2024).

[47]W. H. Tan and S. Takeuchi, Proc. Natl. Acad. Sci. **104**, 1146–1151 (2007).

[48]M. Xu, X. Zhang, Y. Bai, X. Wang, J. Yang, and N. Hu, APL Bioeng. **8**, 026103 (2024).

[49]J. M. Barnes, J. T. Nauseef, and M. D. Henry, PLoS One **7**, e50973 (2012).

[50]M. A. Chiapperino, L. Mescia, P. Bia, B. Staresinic, M. Cemazar, V. Novickij, A. Tabasnikov, S. Smith, J. Dermol-Cerne, and D. Miklavcic, IEEE Trans. Biomed. Eng. **67**, 2781–2788 (2020).

[51]C. Li, Q. Ke, C. Yao, Y. Mi, H. Liu, Y. Lv, and C. Yao, PLoS ONE **13**, e0197167 (2018).